Available online at www.sciencedirect.com
ScienceDirect
Comput. Methods Appl. Mech. Engrg. 386 (2021) 114094
Computer methods in applied mechanics and engineering
www.elsevier.com/locate/cma

Radial and three-dimensional nonlocal pseudopotential calculations in gradient-corrected Kohn–Sham density functional theory based on higher-order finite element methods

İ. Temizer

Department of Mechanical Engineering, Bilkent University, 06800 Ankara, Turkey

Received 3 March 2021; received in revised form 15 June 2021; accepted 1 August 2021
Available online 31 August 2021

Abstract

Kohn–Sham density functional theory is an *ab initio* framework for electronic structure calculation that offers a basis for nonphenomenological multiscale approaches. In this work, higher-order finite element methods are applied in the context of this theory, with a particular focus on the use of nonlocal pseudopotentials. Specifically, an accurate class of pseudopotentials which are based on the generalized gradient approximation of the exchange–correlation functional with nonlinear core corrections are targeted. To this end, the suitable weak formulation of the underlying nonlinear eigenvalue problem is derived and additionally cast in a radial form. The weak forms are discretized through traditional Lagrange elements in addition to isogeometric analysis based on B-splines in order to explore alternative means of achieving faster routes to the solution of the resulting generalized eigenvalue problems with $\mathcal{O}(10^6$–$10^7)$ degrees of freedom. Numerical investigations on single atoms and larger molecules validate the computational framework where stringent accuracy requirements are met through convergence at optimal rates.

Keywords: Kohn–Sham density functional theory; Nonlocal pseudopotentials; Higher-order finite element methods; Isogeometric analysis; Generalized eigenvalue problems

1. Introduction

Multiscale analysis aims at a nonphenomenological understanding of macroscopic physics through fundamental microscopic modeling. Reaching across a hierarchy of scales within this endeavor, one arrives at the atomic level that ultimately determines the mechanics of materials and interfaces. The interactions at this scale are solely governed by the electronic structure and *ab initio* methods aim at its accurate calculation together with the corresponding total energy that gives access to a broad range of properties [1]. A suitable electronic structure calculation method also enables molecular dynamics without the need for empirical potentials [2], thereby offering the possibility of developing predictive frameworks at the next scale towards the continuum [3].

The fundamental role of the electronic structure in this picture led to the development of a great variety of computational frameworks that target nonperiodic systems such as molecules as well as periodic ones such as crystals. Operating within the Born–Oppenheimer approximation where the nuclei are treated classically, it is now

E-mail address: temizer@bilkent.edu.tr.

https://doi.org/10.1016/j.cma.2021.114094
0045-7825/

widely recognized that one suitable theoretical setting for such frameworks towards the prediction of the ground state electronic structure is Kohn–Sham density functional theory [4]. This theory delivers the Kohn–Sham equation, a nonlinear eigenvalue problem in the form of a second-order differential equation, that needs to be solved subject to very stringent accuracy requirements for a large number of eigenpairs. Some of the earliest and most established approaches to address this challenge introduce a basis, such as real-space methods based on Gaussian forms that are mainly targeted for nonperiodic systems and reciprocal-space methods based on plane-waves for periodic systems. Introducing a basis helps preserve the variational structure of density functional theory. However, these early approaches had initial shortcomings which needed to be addressed for enabling large-scale applications. For instance, Gaussian basis sets are not complete and therefore ground state energy cannot be systematically approached, thereby rendering the identification of convergence difficult. On the other hand, plane-waves do offer systematic convergence but cannot provide local resolution control, which is highly desirable for efficient molecular calculations. Despite their perceived shortcomings, these methods remain highly competitive in their respective domains of competence — see [5] for a recent review of various numerical methods. Nevertheless, because the scaling properties of plane-waves are not favorable [6], real-space methods which can offer systematic convergence and are simultaneously applicable to periodic or nonperiodic systems have become appealing [7]. Finite differences, wavelets and finite elements offer three discretization choices towards this purpose [8]. The finite difference method does not introduce a basis, is not variational and offers limited local refinement [9,10]. The wavelet basis delivers a variational approach and also incorporates adaptive local refinement capability through multiple grids [11], leading to highly competitive frameworks [12]. The finite element method (FEM) enables a greater degree of adaptive local refinement capability through graded meshes, a feature that renders it particularly suitable for all-electron calculations with highly variable solutions near atomic cores in addition to pseudopotential calculations where smoother solutions are expected. A review of early works may be found in [13]. The present study will not attempt to simultaneously benefit from all potential advantages of FEM or demonstrate competitiveness with alternative methods — see [14] for a recent set of comparisons. In fact, highly effective real-space methods can be constructed through entirely different routes as well [15]. Instead, the aim will be to expand upon the versatility of the underlying computational framework of FEM by introducing novel theoretical ingredients while simultaneously exploring alternative discretizations.

Since the pioneering application [16] of FEM to Kohn–Sham density functional theory, significant advances have been achieved in this numerical setting, culminating in highly effective computational frameworks [14,17]. Most approaches have predominantly been based on traditional finite element spaces based on hexahedra and tetrahedra. In addition to linear or quadratic discretizations [18–23], the importance of higher-order elements towards achieving higher convergence rates, and hence a greater degree of efficiency with respect to lower-order elements, have emerged within the past ten years [24–27]. All with the exception of [14], these studies invoke a very specific form for the exchange–correlation functional that is central to density functional theory, namely the local density approximation. Because this form remains limited in its predictive capability [28], exploring a class of improved functionals in the context of FEM will be one goal of this current study. Specifically, the implementation of the generalized gradient approximation [29] will be discussed and this implementation will be employed together with a class of nonlocal pseudopotentials [30] that are highly accurate [31].

The emphasis on higher-order finite element discretizations also highlights the need for exploring alternative higher-order discretization spaces that potentially display additional advantages. The framework of isogeometric analysis [32] offers one such alternative. Although its structure differs from the traditional finite element framework in some aspects, notably through the basis structure which is not defined at an element level, this approach will presently be classified as a higher-order FEM based on its many commonalities with the traditional approach both with respect to its computational implementation as well as its mathematical analysis — see [33] for an early survey. One differentiating aspect of isogeometric analysis is the use of discretizations which offer higher-order continuity across the whole domain, an aspect that is particularly suitable to the nature of the solution to the Kohn–Sham equation except at the atomic cores in an all-electron setting. The idea of employing at least C^1-continuous finite element discretizations to capture this smooth solution is not common but also not new [34] — see [35] for a review in a more general context. In fact, cubic Hermite splines have recently been successfully employed in challenging settings [36]. However, achieving similar discretizations at arbitrary orders of continuity is not trivial, and isogeometric discretizations have been instrumental in this respect. Initial efforts have focused on small material systems in nonperiodic [37–41] and periodic [39,42] settings. A nonperiodic framework that is suitable for larger systems has recently been presented in [43] which, as in earlier examples, followed the local density approximation

for the exchange–correlation functional. Therefore, the second goal of this study is to carry out the investigations based on the gradient-corrected functional in the context of higher-order finite element methods which span not only traditional discretizations but also those that are based on isogeometric analysis. It is noted that isogeometric discretizations also allow for local refinement [44–47] but these will not be employed in this work — see [48] for a recent overview with a particular focus on hierarchical B-splines.

The effectiveness of FEM can be improved, in addition to higher-order discretizations with adaptivity, through enrichment. Recently, enriched finite element formulations have been applied to all-electron [49] and nonlocal pseudopotential [50] solutions of the Kohn–Sham equation — see also [51,52] for closely related studies. Here, the solutions to the standard all-electron radial formulation of the Kohn–Sham equation for an atom have been employed in the generation of enrichment functions. For a nonlocal pseudopotential setting, it may be more advantageous to generate the enrichment functions from a suitable radial formulation of the Kohn–Sham equation for an ion. It appears, however, that the formulation of the radial Kohn–Sham equation with nonlocal pseudopotentials is barely discussed in the literature [53] and FEM, which is particularly suitable to its solution, has never been invoked as a solution approach. The third goal of this study is to fill this gap. It is noted that the validation of the three-dimensional FEM framework requires reference nonlocal pseudopotential solutions that can be challenging to calculate even for a single atom if the accuracy sought is very high. The possibility to invoke the developed framework in a radial setting through straightforward manipulations will also deliver extremely accurate solutions which can be employed in single-atom test cases for the validation of three-dimensional finite element implementations.

In order to address the stated goals, the theoretical framework of Kohn–Sham density functional theory will first be outlined in Section 2. Next, in Section 3, the general formulation of nonlocal pseudopotentials will be summarized and the particular formulation to be employed which also complements the nonlinear core correction formulation will be stated. Here, the need for a radial formulation to extract the radial wavefunctions for this class of pseudopotentials will be highlighted. Section 4 will then discuss the Kohn–Sham equation and its three-dimensional weak formulation in the context of the generalized gradient approximation for the exchange–correlation functional. Additionally, a number of algorithmic aspects regarding computational efficiency will be highlighted and the total energy expression will be provided in its final form. The radial counterpart of this formulation, which corresponds to an integrodifferential equation, will be derived in Section 5. Finally, numerical investigations of the computational framework will be presented in Section 6. Here, the ability of the radial formulation to deliver highly accurate reference solutions will be demonstrated and some of these values are subsequently employed in three-dimensional single-atom examples. The investigations will highlight the significant per-degree-of-freedom advantage of B-spline discretizations in comparison to traditional Lagrange discretizations. In all cases, the framework is validated through the demonstration of optimal convergence rates and by comparing the converged values with external references. The investigations are concluded with studies on comparatively large molecules such as cyclo[18]carbon and the buckyball where the solution of generalized eigenvalue problems with $\mathcal{O}(10^6$–$10^7)$ degrees of freedom are needed. In all cases, the ability of the overall framework to satisfy stringent accuracy requirements will be displayed.

2. Kohn–Sham density functional theory

Consider a non-periodic material system consisting of M ions, with positions $\boldsymbol{R}_A$ and ionic charges Z_A ($A \in \{1, 2, \dots, M\}$) in an unbounded space. The position vector will be denoted by $\boldsymbol{r}$, with $r = |\boldsymbol{r}|$ and $\hat{\boldsymbol{r}} = \boldsymbol{r}/r$, through which $\boldsymbol{r}_A = \boldsymbol{r} - \boldsymbol{R}_A$ is also introduced. The ionic charges represent the nuclear charges minus the number of core electrons, which are implicitly treated within the pseudopotential formulation. The presentation focuses on a system with N valence electrons that will be explicitly treated and are associated with a closed-shell atom or molecule but without consideration for spin. Fractional occupancy of its orbitals as well as distinction between spin-up and spin-down configurations are readily incorporated into the theory [1,4]. This extension will be necessary in some of the examples to be presented and will be pursued without a detailed discussion. Introducing generic variables $\{f, x, y\}$, the notation $f[x]$ will be employed to indicate that f is a functional of x whereas $f(y)$ will be employed if f is a function of y and $f[x](y)$ to make such dependencies explicit. Integration over all free coordinates will be indicated by $\langle\cdot\rangle$ and, in view of the real-space formulation pursued within the class of problems considered, all quantities are admitted to be real from the outset. Atomic units are employed throughout this work.

In Kohn–Sham density functional theory based on a nonlocal pseudopotential formulation [1,54], the ground state total energy of the material system is obtained from a functional $E[\boldsymbol{\psi}]$:

$$E = T_s + E_C + E_{xc} + E_{NL} \ . \tag{2.1}$$

Here, the first contribution T_s is associated with the kinetic energy of a non-interacting reference system with N particles. The choice of this reference system allows expressing the valence electron density ρ and T_s exactly through a set $\boldsymbol{\psi}$ of orthonormal spatial orbitals $\psi_i(\boldsymbol{r})$, with the sum running from 1 to $N/2$:

$$\rho(\boldsymbol{r}) = 2\textstyle\sum_i \psi_i^2 \quad , \quad T_s[\boldsymbol{\psi}] = 2\sum_i \langle \psi_i \left(-\frac{1}{2}\nabla^2\right) \psi_i \rangle \ . \tag{2.2}$$

The second contribution to E is the total electrostatic energy E_C of the material system. Following the approaches discussed in [25,55,56], E_C may be expressed as

$$E_C[\rho] = \tfrac{1}{2}\langle (\rho + b)\, v_C \rangle - E_{\text{self}} \ . \tag{2.3}$$

Here, the ionic charge distribution is represented via $b(\boldsymbol{r}) = \sum_{A=1}^{M} \beta_A(\boldsymbol{r})$ where $\beta_A(\boldsymbol{r})$ is a spherically symmetric regularization of the point charge distribution $-\delta(\boldsymbol{r}_A)Z_A$ such that it vanishes or rapidly decays to zero beyond a localized ball around the ion. These distributions can be indirectly defined through a Poisson equation based on the choice of a local part v_A of the pseudopotential for each ion, thereby leading to an expression for the self-interaction energy E_{self} as well:

$$-\tfrac{1}{4\pi}\nabla^2 v_A = \beta_A \quad , \quad E_{\text{self}} = \sum_{A=1}^{M} \tfrac{1}{2}\langle \beta_A\, v_A \rangle \ . \tag{2.4}$$

The total external potential $v_{\text{ext}}[\boldsymbol{b}](\boldsymbol{r}) = \sum_{A=1}^{M} v_A$ helps define the total electrostatic potential $v_C = v_H + v_{\text{ext}}$ appearing within E_C where the Hartree potential $v_H[\rho](\boldsymbol{r})$ as well as v_C satisfy their respective Poisson equations:

$$-\tfrac{1}{4\pi}\nabla^2 v_H = \rho \quad , \quad -\tfrac{1}{4\pi}\nabla^2 v_C = \rho + b \ . \tag{2.5}$$

The third contribution to E is the exchange–correlation energy E_{xc}, which embodies complications associated with electron–electron interactions that are not captured by the remaining terms and, in view of its universal yet elusive dependence on ρ, requires modeling. The exchange–correlation functional is typically expressed through ε_{xc}, the exchange–correlation energy per electron, via $E_{xc}[\rho] = \langle \rho\, \varepsilon_{xc} \rangle$. Without pursuing an explicit decomposition into exchange and correlation contributions, a fundamental choice is the local density approximation (LDA) that is motivated by a uniform density distribution [4], leading to a dependence of ε_{xc} only on ρ. Deviations from uniformity may be handled through an additional dependence on $\nabla\rho$ in the context of the generalized gradient approximation (GGA), the next fundamental choice in a series of increasingly accurate exchange–correlation functionals with respect to predictive capability. The formulation of this dependence is not unique [57]. Based on a widely preferred choice that will be invoked in this work [29], the expression $\varepsilon_{xc}(\rho, \sigma)$ will be employed where $\sigma = |\nabla\rho|^2$. The exchange–correlation functionals are presently implemented using Libxc [58]. Although GGA capability has been reported in a recently released FEM-based software [14], the transition from LDA to GGA requires additional steps that will be pursued in detail for the first time in a modern FEM framework to the best knowledge of the author, which will be addressed in the following sections. An additional minor novelty will be the employment of nonlinear core correction (NLCC) in combination with GGA. NLCC addresses potential errors arising from the nonlinearity of the exchange–correlation functional during the unscreening step of pseudopotential generation [59]. This error can be significant when the core and valence electron densities of an atom significantly overlap and it may be further aggravated during the incorporation of spin [60]. In order to alleviate this error by recapturing the neglected overlap in the context of the frozen core assumption, NLCC introduces a core density $\rho_c(\boldsymbol{r})$ in the evaluation of the exchange–correlation functional in the formulation, leading to the following general expression

$$\overline{\rho} = \rho + \rho_c \quad , \quad E_{xc}[\rho] = \langle \overline{\rho}\, \varepsilon_{xc}(\overline{\rho}, \overline{\sigma}) \rangle \tag{2.6}$$

where the total core charge is a sum of ionic contributions:

$$\rho_c(\boldsymbol{r}) = \sum_{A=1}^{M} \kappa_A(\boldsymbol{r}_A) \ . \tag{2.7}$$

The ion-dependent contributions κ_A are explicitly provided, presently based on the partial core density formulation introduced in [30] where Gaussian forms are employed.

The fourth contribution to E is the nonlocal pseudopotential energy E_{NL}. The interaction of the valence electrons with the frozen cores that are not explicitly accounted for in the pseudopotential formulation determines the local and nonlocal contributions to the total energy [54]. The former is accounted for through the local parts v_A of the ionic pseudopotentials within E_C. The latter is associated with the nonlocal parts Λ_A of the ionic pseudopotentials:

$$v_{NL}(\boldsymbol{r},\boldsymbol{r}') = \sum_{A=1}^{M} \Lambda_A(\boldsymbol{r}_A,\boldsymbol{r}'_A) \quad , \quad E_{NL} = 2\textstyle\sum_i \langle \psi_i(\boldsymbol{r})\, v_{NL}(\boldsymbol{r},\boldsymbol{r}')\, \psi_i(\boldsymbol{r}')\rangle \ . \tag{2.8}$$

The nonlocal pseudopotential is understood to act on a function through integration over $\boldsymbol{r}'$.

3. Nonlocal pseudopotential formulation

Each nonlocal part can be expressed in a generic form that captures a range of widely employed nonlocal pseudopotentials, with the subscript A denoting ion-dependent quantities which are specified as part of the pseudopotential formulation. This form decomposes a nonlocal part into different angular momentum channels $\Lambda^l_A(\boldsymbol{r},\boldsymbol{r}')$, indexed through the azimuthal quantum number $l = 0,\dots,\ell_A$, and each channel is composed of contributions associated with different magnetic quantum numbers $m = -l,\dots,l$:

$$\Lambda_A(\boldsymbol{r},\boldsymbol{r}') = \sum_{l=0}^{\ell_A} \Lambda^l_A(\boldsymbol{r}_A,\boldsymbol{r}'_A) \quad , \quad \Lambda^l_A(\boldsymbol{r}_A,\boldsymbol{r}'_A) = \sum_{m=-l}^{l} Y_{lm}(\hat{\boldsymbol{r}}_A)\, \omega^l_A(r_A,r'_A)\, Y_{lm}(\hat{\boldsymbol{r}}'_A) \ . \tag{3.1}$$

Here, Y_{lm} are the spherical harmonics and ω^l_A is a nonlocal radial function. The form of the nonlocal radial function is the distinguishing feature of the nonlocal pseudopotential. Focusing on norm-conserving nonlocal pseudopotentials [1], examples include: (i) the classical form that is semilocal by construction [61], (ii) its modification into a numerically efficient separable nonlocal form through the Kleinman–Bylander transformation [62] or a direct generation in such a form [63], (iii) a separable form where the nonlocal radial function is composed of multiple projectors [64], instead of one as in earlier forms, either based on the generalized norm-conservation criteria [65] or on a direct generation procedure towards such a form [66]. The last set of examples provides a general form which may be stated through the generic diagonalized expression [64]

$$\omega^l_A(r_A,r'_A) = \sum_{k=1}^{\mathbb{k}_A} p^l_{Ak}(r_A)\, h^l_{Ak}\, p^l_{Ak}(r'_A) \ . \tag{3.2}$$

The radial functions p^l_{Ak}, which vanish or rapidly decay to zero beyond a specified radius around each ion, and the spherical harmonics together constitute the projectors $\lambda^{lm}_{Ak} = p^l_{Ak} Y_{lm}$ which help express the nonlocal ionic pseudopotential in its final form:

$$\Lambda_A(\boldsymbol{r},\boldsymbol{r}') = \sum_{l=0}^{\ell_A} \sum_{m=-l}^{l} \sum_{k=1}^{\mathbb{k}_A} \lambda^{lm}_{Ak}(\boldsymbol{r}_A)\, h^l_{Ak}\, \lambda^{lm}_{Ak}(\boldsymbol{r}'_A) = \sum_{\alpha=1}^{P_A} \lambda_{A\alpha}(\boldsymbol{r}_A)\, h_{A\alpha}\, \lambda_{A\alpha}(\boldsymbol{r}'_A) \ . \tag{3.3}$$

Overall, the constants $\{\ell_A, \mathbb{k}_A, h^l_{Ak}, P_A\}$ are ion-dependent. The latter equality has been introduced as a compact reference to the separable nonlocal nature of the ionic pseudopotential.

The pseudopotential approach initiated in [66] is particularly interesting because it deviates from standard features that are shared by the remaining examples. For instance, the nonlocal radial functions do not vanish beyond a specified radius but rather rapidly decay to zero. Therefore, the resulting wave functions never match their all-electron counterparts perfectly but instead rapidly approach them. More importantly, there is no direct recourse to an atomic solution in the construction of this pseudopotential. Instead, the nonlocal radial functions are based on explicit Gaussian forms, allowing convenient application to both real and reciprocal space calculations, the parameters of which are subsequently optimized for accuracy and transferability. As such, features of the atomic behavior such as radial wavefunctions are not accessible through the form of the pseudopotential without the formulation of an atomic problem. In the radial case, this leads to a nonlinear eigenvalue problem that takes the form of an integrodifferential equation, as first pointed out and solved in [53] and later also in [67]. However, despite its suitability and the elegant

formulation it delivers, FEM has not been applied to the solution of this equation which, therefore, constitutes another goal of this study.

The pseudopotential formulation in [66] was presented with both LDA and GGA parameter sets for selected atoms. The list of atoms was subsequently extended in [68] with LDA parameter sets which additionally incorporate relativistic effects that can optionally be omitted by employing only the scalar parts of the formulation. Further extension to GGA parameter sets was also pursued in [69]. Finally, parameter sets with NLCC for the nonrelativistic formulation were presented in [30], which are to be employed in this work with the updates provided in [70], and have been shown to be highly accurate in comparison to all-electron predictions [31].

4. Three-dimensional Kohn–Sham equation

4.1. Weak form

For density functional theory in the all-electron setting, among all admissible ρ, the ground state density minimizes E. In the Kohn–Sham formalism, this translates into a minimization over the spatial orbitals, a procedure which remains the same in the transition to the nonlocal pseudopotential setting. When subject to the normalization constraint $\langle \psi_i^2 \rangle = 1$ through a corresponding Lagrange multiplier ϵ_i which corresponds to the orbital energy, minimization of (2.1) over ψ_i delivers the canonical Kohn–Sham equation with a nonlocal one-electron Hamiltonian:

$$(-\tfrac{1}{2}\nabla^2 + v_C + v_{xc} + v_{NL})\,\psi_i = \epsilon_i\,\psi_i \ . \tag{4.1}$$

Although the construction of the weak form towards a FEM implementation follows the standard procedure for the Poisson equation $(2.5)_2$ that delivers v_C, the weak form of (4.1) is commented upon due to the contribution from the exchange–correlation potential v_{xc} in the context of GGA. This contribution presently appears symbolically in (4.1) because it is originally defined through its action not on ψ_i but rather on the density variation $\delta\rho$ via $\delta E_{xc} = \langle v_{xc}\,\delta\rho \rangle$:

$$\widetilde{v}_{xc} = \varepsilon_{xc} + \overline{\rho}\,\frac{\partial \varepsilon_{xc}}{\partial \overline{\rho}} \quad , \quad \boldsymbol{w}_{xc} = 2\overline{\rho}\,\frac{\partial \varepsilon_{xc}}{\partial \overline{\sigma}}\nabla\overline{\rho} \quad , \quad v_{xc} = \widetilde{v}_{xc} + \boldsymbol{w}_{xc}\cdot\nabla \ . \tag{4.2}$$

Here, $\widetilde{v}_{xc}$ is the standard LDA term in the context of NLCC while the second term arises from gradient correction. The operation of this second term on ψ_i naturally appears within a weak form and is actually implicit in the derivation of the strong form (4.1). In order to elucidate this aspect, an indirect path is chosen instead based on an intermediate form for the GGA contribution that can be obtained from the minimization statement of the energy, effectively simplifying the direct operation of v_{xc} on ψ_i within the strong form [1]: $\boldsymbol{w}_{xc}\cdot\nabla = -\nabla\cdot\boldsymbol{w}_{xc}$. For the construction of the weak form, it is noted that ψ_i are subject to homogeneous Dirichlet boundary conditions, imposed on sufficiently large domains in a numerical setting. Consequently, introducing a test function $\varphi(\boldsymbol{r})$ and observing $\langle \nabla\cdot(\varphi\,\boldsymbol{w}_{xc}\,\psi_i)\rangle = 0$, the GGA contribution $-\langle \varphi\,\nabla\cdot\boldsymbol{w}_{xc}\,\psi_i\rangle$ to the weak form may be recast in a way that clarifies its operation on ψ_i and additionally highlights the symmetric contribution of the total exchange–correlation potential to the weak form [1]:

$$\langle \varphi\,v_{xc}\,\psi_i\rangle = \langle \varphi\,\widetilde{v}_{xc}\psi_i\rangle + \langle \varphi\,\boldsymbol{w}_{xc}\cdot\nabla\psi_i + \nabla\varphi\cdot\boldsymbol{w}_{xc}\,\psi_i\rangle \ . \tag{4.3}$$

To complete the weak form, the compact representation $(3.3)_2$ is employed to express the nonlocal contribution from the pseudopotential as

$$\langle \varphi\,v_{NL}\,\psi_i\rangle = \sum_{A=1}^{M}\sum_{\alpha=1}^{P_A}\langle \varphi\,\lambda_{A\alpha}\rangle\,h_{A\alpha}\,\langle \lambda_{A\alpha}\,\psi_i\rangle \tag{4.4}$$

which is also observed to be symmetric and leads to the weak form of (4.1) after the standard manipulation of the kinetic energy contribution as well:

$$\tfrac{1}{2}\langle \nabla\varphi\cdot\nabla\psi_i\rangle + \langle \varphi\,(v_C + v_{xc} + v_{NL})\,\psi_i\rangle = \epsilon_i\langle \varphi\,\psi_i\rangle \tag{4.5}$$

In order to construct the discrete counterpart of the weak form (4.5), a set of basis functions N_I is introduced such that a finite element test/trial function v is discretized as $\sum_I v^I N_I$ and $\{w\}$ will indicate the vector associated

with a set of values w^I. Subsequently, the basis-weighted integrals $\overline{\lambda}^I_{A\alpha} = \langle N_I \lambda_{A\alpha} \rangle$ are defined for each projector such that the nonlocal contribution (4.4) takes the discrete form

$$[H_{NL}] = \sum_{A=1}^{M} \sum_{\alpha=1}^{P_A} \{\overline{\lambda}_{A\alpha}\} h_{A\alpha} \{\overline{\lambda}_{A\alpha}\}^T \quad , \quad \langle \varphi \, v_{NL} \, \psi_i \rangle = \{\varphi\}^T [H_{NL}] \{\psi_i\} \, . \tag{4.6}$$

On the other hand, the exchange–correlation contribution (4.3) may be cast as

$$H^{IJ}_{xc} = \langle N_I \, \widetilde{v}_{xc} N_J \rangle + \langle N_I \, \boldsymbol{w}_{xc} \cdot \nabla N_J + \nabla N_I \cdot \boldsymbol{w}_{xc} \, N_J \rangle \quad , \quad \langle \varphi \, v_{xc} \, \psi_i \rangle = \{\varphi\}^T [H_{xc}] \{\psi_i\} \, . \tag{4.7}$$

It is noted that the use of GGA in a finite element setting has recently been reported in [14], although details of implementation were not provided. Indeed, the form of the exchange–correlation contribution to the discrete Hamiltonian provided therein is not compatible with the GGA formulation above without further manipulation. However, the software presented in [14] is a functional finite element framework from which the details of the specific GGA implementation pursued therein may be extracted — see also [71] for a GGA-based application of this software.

Defining the remaining standard contributions to the discrete Hamiltonian associated with kinetic energy and electrostatics in addition to the overlap matrix $[M]$ as

$$H^{IJ}_T = \tfrac{1}{2} \langle \nabla N_I \cdot \nabla N_J \rangle \quad , \quad H^{IJ}_C = \tfrac{1}{2} \langle N_I \, v_C \, N_J \rangle \quad , \quad M^{IJ} = \langle N_I N_J \rangle \tag{4.8}$$

one obtains the discrete form of the Kohn–Sham equation (4.1) with a symmetric discrete Hamiltonian $[H]$:

$$[H] = [H_T] + [H_C] + [H_{xc}] + [H_{NL}] \quad , \quad [H]\{\psi_i\} = \epsilon_i [M] \{\psi_i\} \, . \tag{4.9}$$

4.2. Solution scheme

The solution scheme that is applied towards the solution of the discrete Kohn–Sham equation will closely follow the choices in [43]. In this section, a number of differences and improvements are briefly commented upon.

Because $[H_C]$ and $[H_{xc}]$ depend on $\{\psi_i\}$ through the electron density ρ, (4.9) is a nonlinear generalized eigenvalue problem that needs to be solved in combination with the discrete counterpart of the Poisson equation $(2.5)_2$ through self-consistent field iterations within a suitable mixing scheme applied on the density. Presently, the Anderson scheme will be employed [1] and, for consistency, mixing is applied in an identical fashion on the density gradient as well in view of the GGA setting.

Within such an iterative scheme, convergence can be accelerated with a good initial guess for the orbitals $\{\psi_i\}$. Presently, the iterations are initiated on a coarse mesh with a guess that is based on atomic solutions, for instance those that are obtained through the radial formulation that will be discussed shortly. During mesh refinement towards convergence, the coarser mesh solution is subsequently mapped onto the finer mesh through L_2-projection to generate the updated initial guess. It was found that such a choice greatly accelerates convergence and leads to only a few iterations at sufficiently fine resolutions near the target accuracy requirements. When generating the types of convergence plots to be presented in Section 6 or in attempting to assess whether target accuracy requirements are met in the absence of an external comparison value, this choice clearly reduces overall calculation times as well. However, it may not necessarily lead to a reduction if the only aim is to extract the energy associated with a certain resolution, either because the coarse mesh solution is not sufficiently accurate to accelerate convergence or because the accumulated time towards the target resolution exceeds the time associated with a direct initiation at this resolution.

At each iteration, a generalized eigenvalue problem must be solved where the Hamiltonian is symmetric and the overlap is symmetric positive-definite. For the large-scale standard eigenvalue problems that are addressed in density functional theory calculations where $\mathcal{O}(10^6$–$10^7)$ degrees of freedom are easily encountered, the Chebyshev-filtered subspace iteration method [72,73] has emerged as a leading approach over the past ten years [15,25,74]. Presently, this method is adapted to the generalized eigenvalue problem setting through the application of the opening and closing steps in the method, namely the Lanczos and the Rayleigh–Ritz algorithms, in a generalized format [75]. The core step in the method, on the other hand, is the Chebyshev polynomial filtering step that entails recursive application of $[M]^{-1}[H]$ on a set of vectors that span the subspace within which $\{\psi_i\}$ are sought. As highlighted earlier, the nonlocal pseudopotentials of [66] employed in this work do not vanish beyond a specified radius around

an ion. Without a cut-off on the components of $[H_{NL}]$, this feature leads to a dense Hamiltonian matrix. However, the value of a suitable cut-off tolerance is dependent on the accuracy sought. In order to eliminate this arbitrariness, the separable nature of the nonlocal pseudopotentials is recognized. Indeed, because the action of $[H_{NL}]$ on a vector is easily obtained through the expression (4.6), a cut-off is not required. All the components of the vectors $\{\bar{\lambda}_{A\alpha}\}$ can be calculated irrespective of their magnitude and, subsequently, the action of $[H]$ on a generic vector $\{v\}$ can be decomposed into two steps and summing their results: (1) the action of $[H_T] + [H_C] + [H_{xc}]$ on $\{v\}$ which requires the assembly of these contributions, accompanied by (2) the action of $[H_{NL}]$ on $\{v\}$, namely $[H_{NL}]\{v\} = \sum_{A=1}^{M} \sum_{\alpha=1}^{P_A} \{\bar{\lambda}_{A\alpha}\} h_{A\alpha} (\{\bar{\lambda}_{A\alpha}\}^T \{v\})$, which does not require assembly. The calculations carried out in this work indicate that this choice leads to negligible change in calculation times in comparison to the approach where a judiciously chosen cut-off is applied to $[H_{NL}]$ during assembly in order not to compromise its sparsity while ensuring a desired accuracy. The clear advantage is that the nonlocal pseudopotentials of [66] can now be represented very precisely on a given mesh.

4.3. Energy expression

When employed together with $(2.2)_2$, (4.1) allows expressing the total energy as

$$E = 2\sum_i \epsilon_i - \langle \rho\, (v_C + v_{xc}) \rangle + E_C + E_{xc} \tag{4.10}$$

where, in view of $(2.2)_1$ and (4.3),

$$\langle \rho\, v_{xc} \rangle = \langle \rho\, \widetilde{v}_{xc} \rangle + \langle \boldsymbol{w}_{xc} \cdot \nabla \rho \rangle \tag{4.11}$$

and the explicit appearance of E_{NL} is eliminated through a corresponding contribution from v_{NL} within T_s. In order to address open-shell problems and degenerate orbital energies, (4.10) will additionally be extended to fractional occupancy of the orbitals through finite-temperature smearing — see [25] for a summary of the algorithmic details. The latter can be incorporated in (2.2) and (4.10) through orbital occupancy factors $f_i \in [0, 1]$, leading to

$$\rho(\boldsymbol{r}) = 2\sum_i f_i \psi_i^2 \quad , \quad E = 2\sum_i f_i \epsilon_i - \langle \rho\, (v_C + v_{xc}) \rangle + E_C + E_{xc} \tag{4.12}$$

More specifically [1,4,76], the free energy $\mathcal{E} = E - \theta S_s$ is introduced where θ is the temperature and S_s is the entropy of the reference Kohn–Sham system

$$S_s = -2k \sum_i \{ f_i \ln f_i + (1 - f_i) \ln (1 - f_i) \} \tag{4.13}$$

with k as the Boltzmann constant. Incorporating the normalization constraint together with the summation constraint $2\sum_i f_i = N$, which is enforced through a Lagrange multiplier ϵ_F, the stationary point of the functional

$$\mathcal{F} = \mathcal{E} + 2\sum_i f_i \epsilon_i \, (1 - \langle \psi_i^2 \rangle) + \epsilon_F \, (N - 2\sum_i f_i) \tag{4.14}$$

delivers (4.1) as well as the Fermi–Dirac distribution $f_i = [1 + \exp \frac{\epsilon_i - \epsilon_F}{k\theta}]^{-1}$ where ϵ_F appears as the Fermi energy. Presently, smearing is only employed as a numerical tool to estimate the zero-temperature properties of the system, in particular to minimize E [77].

5. Radial formulation with nonlocal pseudopotentials

The expression of the total energy $(4.12)_2$ remains identical in the transition to the radial case which addresses a single atom possessing a spherical density [43]. Relevant Poisson problems also retain their forms, with ∇^2 replaced by $\nabla_r^2 = r^{-2}(r^2(\cdot)')'$ where $(\cdot)' = \frac{\mathrm{d}(\cdot)}{\mathrm{d}r}$. In the case of a purely local pseudopotential, the derivation of the radial Kohn–Sham equation from its three-dimensional counterpart (4.1) follows the classical outline [78]. In the presence of nonlocal contributions to the pseudopotential, on the other hand, the classical approach requires modification in order to obtain the form stated in [53]. To this end, let $\nabla^2 = \nabla_r^2 + r^{-2}\nabla_s^2$, which defines ∇_s^2 as the Laplacian on the unit sphere. The solution is assumed and indexed in the form $\psi_{nlm}(\boldsymbol{r}) = R_{nl}(r) Y_{lm}(\widehat{\boldsymbol{r}})$ where $n = 1, 2, \ldots$ is the principal quantum number and $l = 0, 1, \ldots, n-1$ so that (4.1) simplifies to

$$-\tfrac{1}{2}(Y_{lm}\nabla_r^2 R_{nl} + r^{-2} R_{nl} \nabla_s^2 Y_{lm}) + (v_C + v_{xc}) R_{nl} Y_{lm} + v_{NL} R_{nl} Y_{lm} = \epsilon_{nl} R_{nl} Y_{lm} \, . \tag{5.1}$$

Note that equal fractional occupancy is assumed for degenerate solutions associated with $m = -l, \ldots, l$ in order to ensure a spherical density. Also, only a single energy level n will be occupied in the nonlocal pseudopotential

solutions of this work and the value of this level will be indicated as the valence value from the corresponding all-electron setting. Recalling the representation $(3.3)_1$ with the subscript A dropped because there is a single atom, the nonlocal contribution from the ionic pseudopotential can be expressed as

$$v_{NL} R_{nl} Y_{lm} = \sum_{l'=0}^{\ell} \sum_{m'=-l'}^{l'} \sum_{k=1}^{\mathbb{k}} p_k^{l'} Y_{l'm'} \, h_k^{l'} \, \langle p_k^{l'} R_{nl} \rangle_r \langle Y_{l'm'} Y_{lm} \rangle_s = \sum_{k=1}^{\mathbb{k}} p_k^l Y_{lm} \, h_k^l \, \langle p_k^l R_{nl} \rangle_r \tag{5.2}$$

where $\langle \cdot \rangle_r = \langle \cdot \, r^2 \rangle$ denotes radial integration, $\langle \cdot \rangle_s$ denotes integration on the unit sphere and the orthonormality condition $\langle Y_{l'm'} Y_{lm} \rangle_s = \delta_{l'l} \delta_{m'm}$ has been invoked. Employing the eigenvalue property $\nabla_s^2 Y_{lm} = -l(l+1) Y_{lm}$ with the accompanying centrifugal term definition $v_l = \frac{l(l+1)}{2r^2}$, multiplying (5.1) with Y_{lm} and integrating over the unit sphere, one obtains the integrodifferential equation in [53] that is subject to the normalization constraint $\langle R_{nl}^2 \rangle_r = 1$:

$$-\tfrac{1}{2} \nabla_r^2 R_{nl} + (v_l + v_C + v_{xc}) R_{nl} + \textstyle\sum_{k=1}^{\mathbb{k}} p_k^l \, h_k^l \, \langle p_k^l R_{nl} \rangle_r = \epsilon_{nl} R_{nl} \ . \tag{5.3}$$

The radial Kohn–Sham equations for all occupied values of l must be solved self-consistently, together with the radial Poisson equation for v_C. Following steps which are similar to the three-dimensional case, the weak form of (5.3) can be obtained through a radial test function $\varphi(r)$:

$$-\tfrac{1}{2} \langle \varphi' R_{nl}' \rangle_r + \langle \varphi \, (v_l + v_C + v_{xc}) R_{nl} \rangle_r + \textstyle\sum_{k=1}^{\mathbb{k}} \langle \varphi \, p_k^l \rangle_r \, h_k^l \, \langle p_k^l R_{nl} \rangle_r = \epsilon_{nl} \langle \varphi R_{nl} \rangle_r \ . \tag{5.4}$$

The accompanying finite element formulation based on this symmetric weak form delivers an efficient solution of the atomic problem with a nonlocal pseudopotential. Note that the presence of v_{xc} in the context of a GGA contribution is handled without difficulty also in the radial setting because the density renders it spherical as well and a similar weak form implementation follows in terms of R_{nl}:

$$w_{xc} = 2\overline{\rho} \, \frac{\partial \varepsilon_{xc}}{\partial \overline{\sigma}} \overline{\rho}' \quad , \quad \langle \varphi \, v_{xc} \, R_{nl} \rangle_r = \langle \varphi \, \widetilde{v}_{xc} \, R_{nl} \rangle_r + \langle \varphi \, w_{xc} \, R_{nl}' + \varphi' \, w_{xc} \, R_{nl} \rangle_r \ . \tag{5.5}$$

6. Numerical investigations

6.1. Discretization and accuracy

Towards the calculation of the total energy, the Poisson and Kohn–Sham equations will be solved within a standard Bubnov–Galerkin finite element discretization. In particular, both Lagrange and B-spline basis functions will be employed, the former referring specifically to standard hexahedral elements. For a given order p, discretizations based on Lagrange basis functions will be indicated by $\mathcal{L}^p$ and those based on B-splines by $\mathcal{B}^p$. Linear Lagrange and B-spline discretizations are equivalent and will be indicated by $\mathcal{L}^1$. Due to the combination of its variational structure and the underlying discretization, FEM delivers systematic convergence towards the ground state energy through monotonic reduction in the total energy with mesh refinement. For a given reference ground state energy E_o which will be predicted on a fine discretization, this systematic convergence will be demonstrated through the asymptotic expression for the error $E - E_o$:

$$E - E_o = C h^{2k} \ . \tag{6.1}$$

Among the constants C and k, the latter is ideally equal to the order p of the discretization. The numerical value of k will be predicted through the last three points on a series of successive mesh refinements and compared against p in order to validate the FEM framework. The resolution of the discretization is controlled by a refinement parameter e_o that delivers the element size h and the number of degrees of freedom n_{dof}. Specifically, in the radial setting, the mesh will be composed of two parts: a core mesh where the element size is uniform and an outer mesh where the element size is graded in order to resolve the vacuum. Both meshes are assigned e_o elements, leading to $n_{dof} \approx 2e_o$. For B-spline discretizations, the order can be varied independently of e_o so that $n_{dof} = 2(e_o + p - 1)$. For Lagrange discretizations, e_o will stand for the number of linear elements which can then be merged into elements of higher order so that $n_{dof} = 2e_o$ holds irrespective of the order. A similar mesh structure is employed in the three-dimensional setting as well (Fig. 1).

Unless otherwise noted, only the GGA functional will be employed together with NLCC in all following examples based on the references earlier provided. When the nonlocal contributions to the Kohn–Sham equation as well as to the total energy are omitted together with the NLCC contribution to the charge density and the regularized

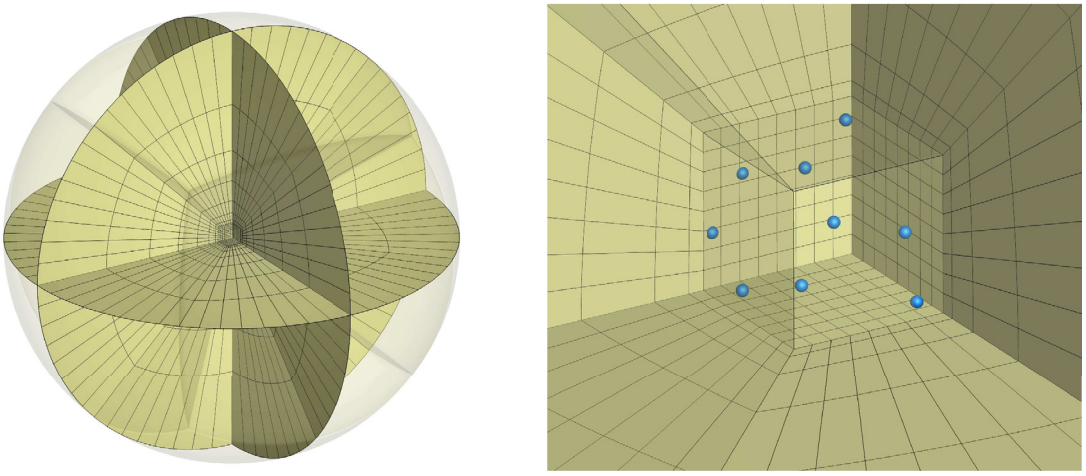

(a) domain geometry with mesh grading (b) uniform mesh of the core region

Fig. 1. The three-dimensional mesh structure is summarized. In the close-up view, the blue spheres indicate a portion of the ions in the buckyball molecule. In the radial setting, the mesh structure follows any one of the edges from the vertex of the core region.

ionic charges are replaced by point nuclear charges, the all-electron case is obtained. This setup will additionally be employed for demonstrating the implementation of the GGA functional. In all radial calculations, the calculated reference values are converged to 10^{-10} accuracy with respect to domain size and to 10^{-11} with respect to resolution, with the exception of the aluminum all-electron example where the latter accuracy is also 10^{-10}. For further validation of the results, comparison calculations will be carried out. For the all-electron (AE) case, the atomic program from [79] (to be referred to as ATOM) will be employed, obtaining results which are converged to 10^{-9} accuracy with respect to domain size and resolution. For the nonlocal pseudopotential (PP) setting, ABINIT [80] and BigDFT [81] will be employed in order to obtain results with 10^{-6} accuracy, for the former with respect to cell size as well as energy cut-off and for the latter with respect to grid refinement in a free atom calculation. These two programs are designed for general three-dimensional nonlocal pseudopotential studies and, as such, take orders of magnitude larger time to deliver a single-atom result that is of comparable accuracy to the radial formulation presented here. Effort is made to ensure agreement between the reference and comparison values to the available accuracy.

6.2. Radial studies

6.2.1. All-electron calculations

The first demonstration of the radial case will be on the lithium atom in an all-electron setting. The calculated reference value is $E_o = -7.451\,372\,042\,03$ and the comparison value from ATOM is $-7.451\,372\,042$. Results in Fig. 2(a) demonstrate predictions of the convergence rates that are observed to be nearly optimal for each discretization type. Additionally, B-spline basis functions are always significantly more accurate on a given resolution, compared to Lagrange basis functions of the same order. In fact, the $\mathcal{B}^3$ discretization is outstanding in terms of accuracy when compared to all other Lagrange discretizations, here limited to fifth order. Similar observations also hold when spin-up and spin-down occupancy of the orbitals is distinguished, as demonstrated in Fig. 2(b), where the calculated reference value is $E_o = -7.462\,180\,386\,79$ and the comparison value from ATOM is $-7.462\,180\,387$.

In remaining radial studies, spin will not be accounted for and only B-splines will be employed. With this choice, the FEM implementation of the all-electron setting with GGA is additionally demonstrated using carbon and aluminum atoms in Fig. 3. The reference (comparison) values are $-37.748\,208\,778\,92$ ($-37.748\,208\,779$) and $-242.224\,964\,048\,3$ ($-242.224\,964\,048$) for carbon and aluminum, respectively. Finer resolutions are required to achieve a given accuracy for increasing atomic number. Considering that discretizations for $e_o = 24$ have only about 50 degrees of freedom, the accuracy provided by B-splines is observed to be remarkable and can help efficiently represent enrichment functions for use in three-dimensional calculations.

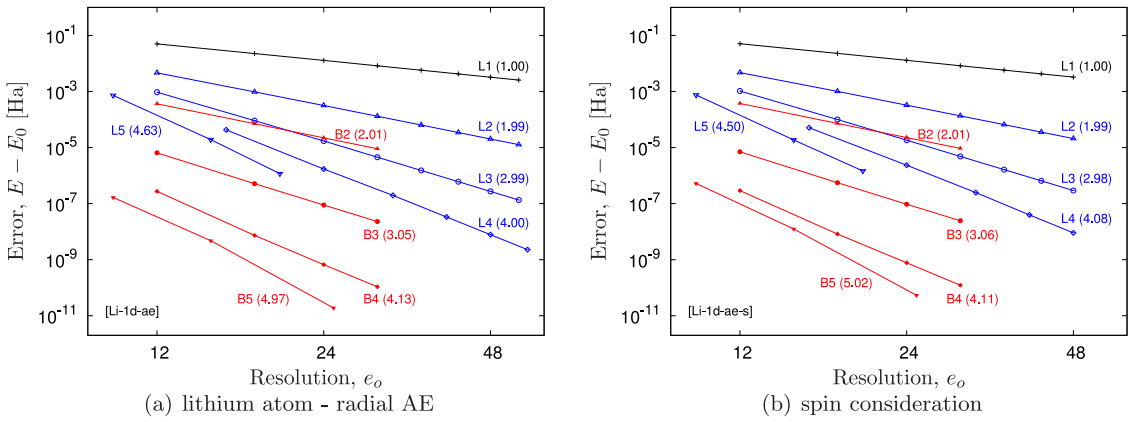

(a) lithium atom - radial AE (b) spin consideration

Fig. 2. Radial AE computations on the lithium atom are summarized. The prediction for the convergence rate (k) is indicated in parentheses for each set of points belonging to a discretization choice, which are connected with a line for clarity.

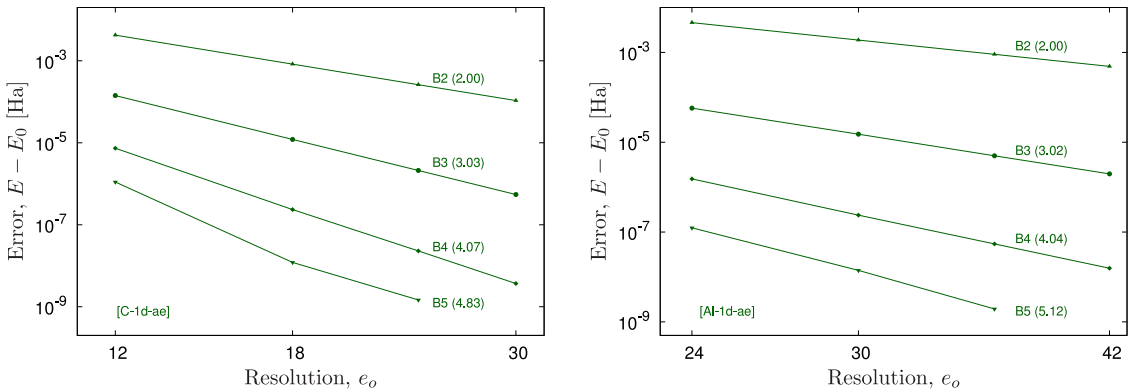

(a) carbon atom - radial AE (b) aluminum atom - radial AE

Fig. 3. Radial AE computations on carbon and aluminum atoms are summarized.

6.2.2. Nonlocal pseudopotential calculations

Lithium atom is chosen again as the first example for the radial pseudopotential studies. For the default setting, the calculated reference value is $E_o = -0.348\,890\,083\,64$. The comparison values for this setting will be obtained from BigDFT and for lithium it is $-0.348\,890$. Only this example is also carried out with the LDA parameter set in [68] without NLCC. The calculated reference value is $E_o = -0.189\,548\,269\,38$ and the comparison value is obtained from ABINIT as $-0.189\,548$. The results in Fig. 4 demonstrate optimal convergence rates, thereby validating the FEM framework in the radial nonlocal pseudopotential setting as well. Here, the $\mathcal{B}^5$ discretization already achieved results of comparable magnitude to the reference value at very low resolution so that only a single point has been shown.

The radial nonlocal pseudopotential setting is also demonstrated for the carbon and aluminum atoms. The calculated reference values for these are, respectively, $-6.243\,608\,042\,02$ and $-4.753\,770\,322\,54$ whereas the comparison values are $-6.243\,608$ and $-4.753\,770$. These results further demonstrate the even higher accuracy of B-splines in the nonlocal pseudopotential setting. This accuracy can be employed to efficiently represent enrichment functions for three-dimensional nonlocal pseudopotential studies. The orbitals which would be employed in the construction of such enrichment functions are visualized in Fig. 6 for aluminum. The radial functions of the pseudopotential solution rapidly approach the valence ($n = 3$) orbitals of the all-electron setting, which is required in view of the norm-conserving property of the nonlocal pseudopotential employed.

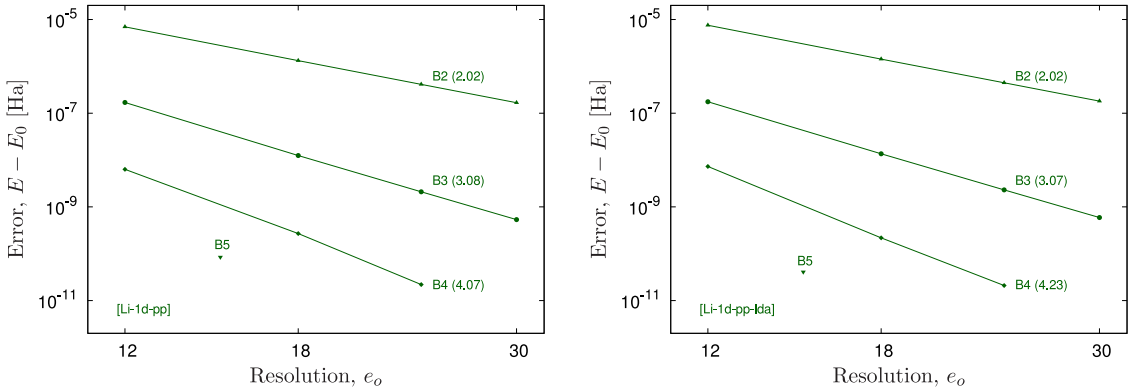

(a) lithium atom - radial nonlocal PP (b) LDA parameter set

Fig. 4. Radial nonlocal PP computations on the lithium atom are summarized.

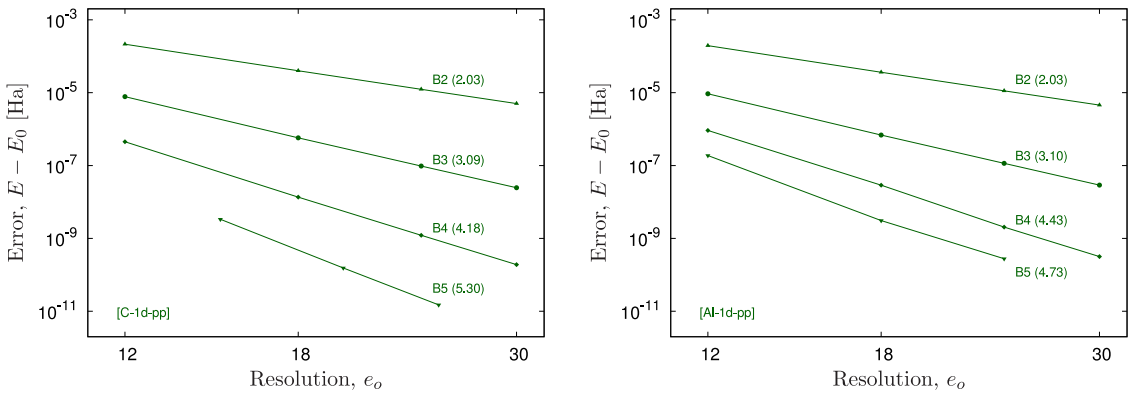

(a) carbon atom - radial nonlocal PP (b) aluminum atom - radial nonlocal PP

Fig. 5. Radial nonlocal PP computations on the carbon and aluminum atoms are summarized.

6.3. Three-dimensional studies

6.3.1. Single-atom calculations

In three-dimensional studies, the discretization setup follows the radial one such that a uniform core mesh is surrounded by a graded outer mesh. Presently, the boundary of the outer mesh has been chosen to match a spherical geometry as closely as possible even on a coarse discretization, which required employing NURBS outside the core region. However, this choice is not necessary and it can be demonstrated that using B-splines instead leads to insignificant changes. This is because the outer mesh mainly serves the purpose of resolving the vacuum whereas the accuracy is mainly controlled by the core mesh where only B-splines are employed. Consequently, the notation $\mathcal{B}^p$ will again be employed to refer to isogeometric discretizations. Only cubic and quartic discretizations will be displayed in the results because, as demonstrated in Fig. 2 as well, these choices can effectively compete with higher-order Lagrange discretizations in a broad range of scenarios.

Towards the validation of the three-dimensional framework, nonlocal PPs will be employed in the default GGA setting together with NLCC. To this end, the single-atom studies of Fig. 5 are revisited as a first step and their three-dimensional counterparts are summarized in Fig. 7. Here, the reference values are borrowed from the radial calculations and the resolution is indicated with the number of degrees of freedom in order to highlight typical computational costs. The per-atom total energy error in AE studies is targeted to be below the chemical accuracy of 1 kcal/mol ($\approx$0.0016 Ha). In PP studies, the required accuracy is typically about an order of magnitude smaller and is presently chosen as 0.1 kcal/mol. These accuracy targets are additionally displayed on the figures. Despite

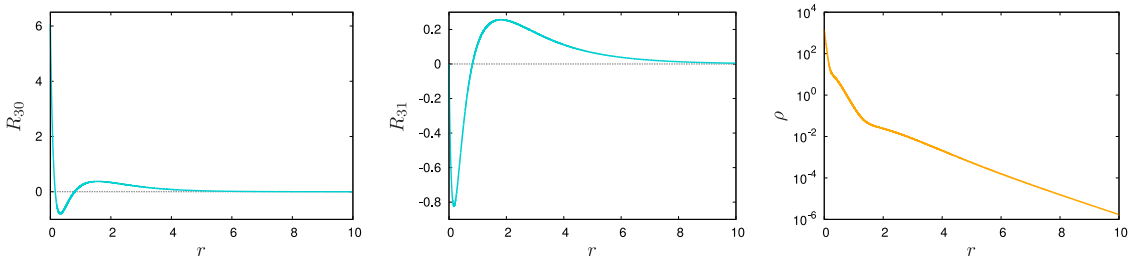

(a) valence AE orbitals and the electron density

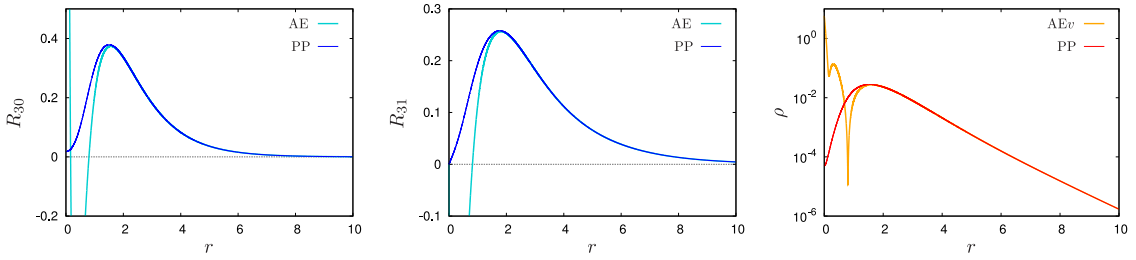

(b) PP orbitals and the electron density

Fig. 6. The valence AE and radial PP solutions for the aluminum atom are visualized, both in the context of the default GGA setting and the latter also incorporating NLCC. In the density plot for the PP setting, the AE density distribution is associated only with the valence orbitals and hence is marked with "v".

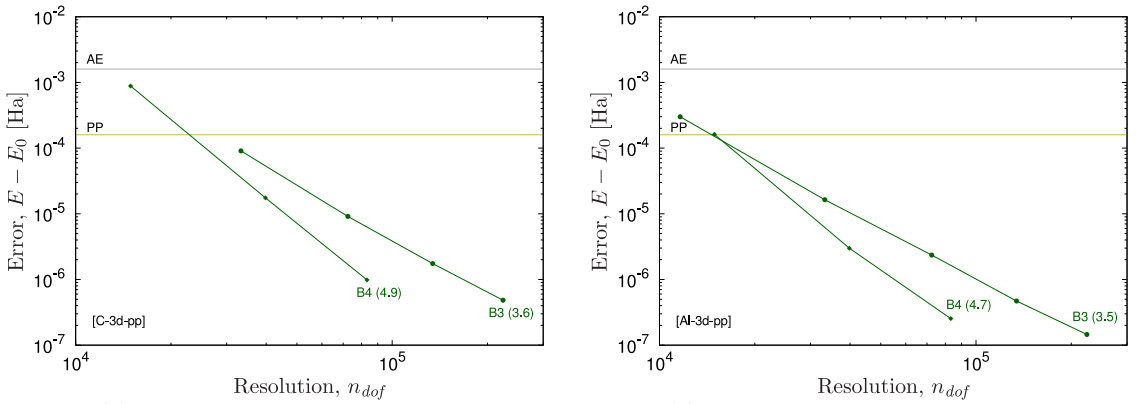

(a) carbon atom - radial nonlocal PP (b) aluminum atom - radial nonlocal PP

Fig. 7. Three-dimensional nonlocal PP computations on the carbon and aluminum atoms are summarized.

the simple mesh construction where the uniform core mesh dominates the error, very high accuracies can easily be attained in single-atom studies. This simple mesh construction influences the pre-asymptotic convergence rates and deviations from the optimal values can be observed [43]. Presently, similar to various radial results presented earlier, these rates fall in the super-optimal range and are indicative of the advantages of increasing discretization order.

6.3.2. Molecular calculations

Two molecular examples are considered in this section. The first one is the cyclo[18]carbon molecule [82], based on the polyynic geometry reported in [83] where 18 carbon ions are located on a circle of radius 3.6873 Å with alternating bond lengths of 1.362 Å and 1.199 Å. The reference total energy calculated with BigDFT is E_o =

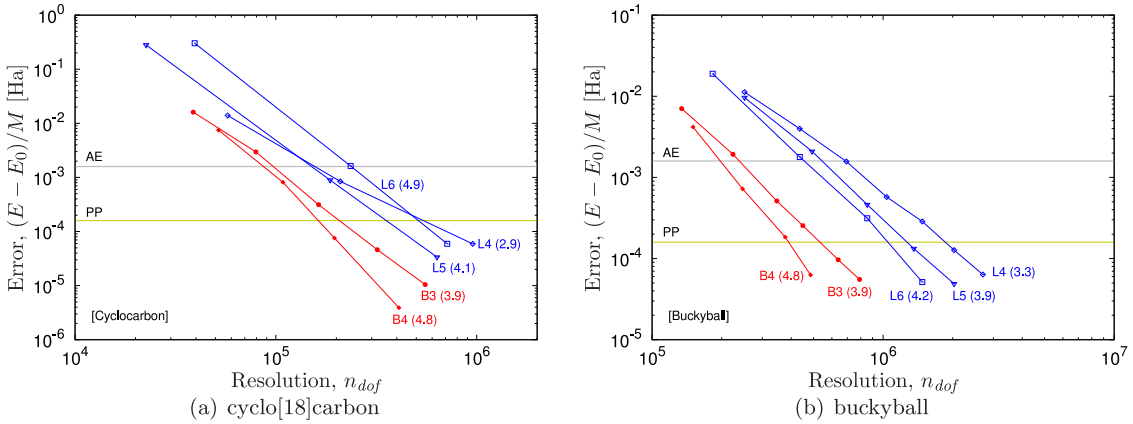

Fig. 8. Nonlocal PP computations on cyclo[18]carbon and buckyball molecules are summarized.

-117.71503 Ha to 10^{-5} accuracy. The second one is the buckyball molecule where 60 carbon ions are located on a truncated icosahedron geometry with an encapsulating sphere that is assigned a radius of 3.5244 Å. The reference total energy from BigDFT is $E_o = -394.1319$ Ha to 10^{-4} accuracy. It is noted that this example was considered with B-spline discretizations earlier in [43] in an LDA setting, but it was not possible to approach these stringent accuracy requirements. In the present GGA setting with NLCC, due to algorithmic improvements mentioned earlier, accuracies that lie well beyond the target values have been attained in all discretization choices.

Due to the planar geometry of the first example, the length of the core mesh in the out-of-plane direction was chosen to be smaller than the in-plane dimensions for numerical efficiency. As a consequence, it was not possible to perfectly preserve the element aspect ratio during mesh refinement in some of the discretization choices. Although deviations from the initial aspect ratio were very small when they occurred, all the data points available were employed for this example in the estimation of the convergence rates to partially alleviate any potential influence. For consistency, a similar approach was employed in the second example as well. The results in Fig. 8 again demonstrate the favorable convergence rates of cubic and quartic B-spline discretizations. Here, Lagrange discretizations have once again been incorporated for comparison purposes. The well-established per-degree-of-freedom advantage of B-spline discretizations is evident in these results as well. It is worth noting that the time-to-solution aspect is an additional practical measure of interest. Although a detailed comparison of calculation times is not a goal of the present study, results indicate that comparable accuracies typically require times at the same order of magnitude for Lagrange and B-spline discretizations, with the former choice usually displaying smaller per-iteration time despite requiring a larger number of degrees of freedom — see Appendix for a representative analysis. Finally, the electron density distributions for these examples are shown in Fig. 9 where it is observed that not all bonds are equal. Indeed, the alternating density distribution for cyclo[18]carbon is consistent with the polyynic structure reported in [82] and the similar variation throughout the buckyball is associated with the presence of rings that alternate between hexagons and pentagons.

7. Conclusion

The finite element method presents a powerful alternative to established electronic structure calculation methods in the context of the Kohn–Sham density functional theory. Through its variational structure combined with a methodological refinement scheme, it offers systematic convergence towards the ground state energy. The element-based discretization along with the sparse matrix structure which emanates from it endows this real-space approach with good parallelization properties. The importance of employing higher-order discretizations in the context of the finite element method has been highlighted over the past years. In this work, building upon recent studies, such discretizations have been investigated both through traditional Lagrange as well as more recent isogeometric choices. Specifically, the studies have concentrated on introducing a class of accurate and highly transferable nonlocal pseudopotentials into the finite element setting based on the generalized gradient approximation of the exchange–correlation functional together with nonlinear core correction. In addition to the discussion of the three-dimensional

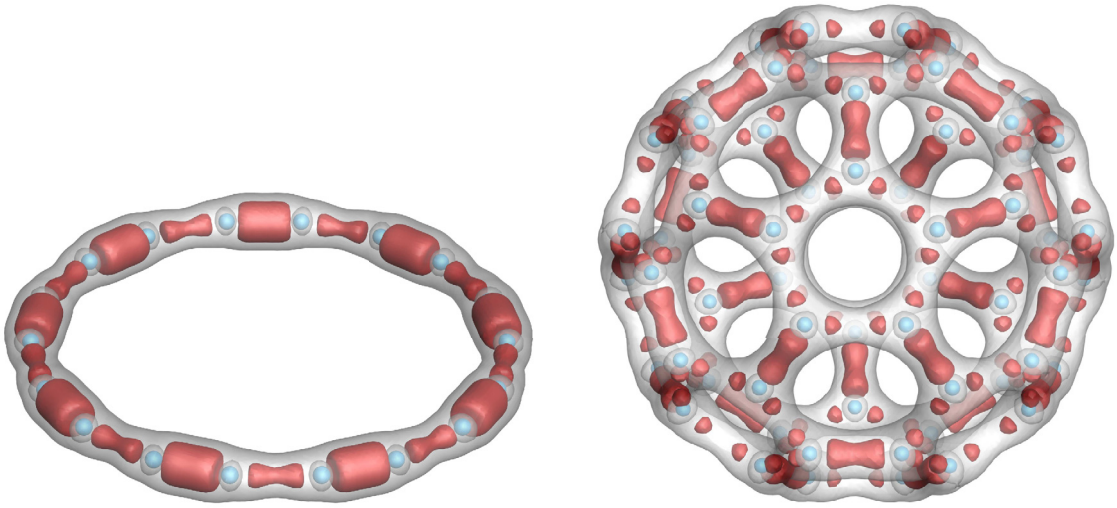

(a) cyclo[18]carbon (b) buckyball

Fig. 9. The electron density isosurfaces for cyclo[18]carbon and buckyball molecules are displayed (outer/gray: 0.22, inner/red: 0.3) with the blue spheres indicating the carbon ions. Both plots are associated with $\mathcal{B}^3$ discretizations which deliver a per-atom error that is below the target PP accuracy at 235,893 and 638,821 degrees of freedom, respectively. (For interpretation of the references to color in this figure legend, the reader is referred to the web version of this article.)

finite element implementation of this approach, the radial formulation has also been derived in order to enable the efficient extraction of the atomic orbitals. Through a series of algorithmic improvements, the ability of this approach to effectively satisfy stringent accuracy requirements has additionally been shown.

Among higher-order discretization choices, B-splines display their well-established per-degree-of-freedom accuracy advantage in this setting as well [33]. In order to fully harness this advantage and reflect it towards calculation times, the generalized setting of the discrete eigenvalue problem is an outstanding challenge that needs to be addressed. Based on the use of spectral elements, it is possible to effectively convert this problem to the standard setting in the context of Lagrange-type discretizations [25]. A comparable treatment of isogeometric discretizations towards a standard setting without compromising convergence rates would deliver significant computational gains. A faster core algorithm for reaching the ground state energy within tight error bounds is crucial towards optimization for predicting equilibrium molecular geometries and will also enable carrying out *ab initio* molecular dynamics based on the investigated computational framework.

Declaration of competing interest

The authors declare that they have no known competing financial interests or personal relationships that could have appeared to influence the work reported in this paper.

Acknowledgment

Support for this work was provided by the Scientific and Technological Research Council of Turkey (TÜBİTAK) under the 1001 Programme (Grant No. 119M981).

Appendix. Calculation times

In this section, indicative results are presented as a representative analysis of major factors which influence the calculation times mentioned in Section 6.3.2. To this end, the buckyball molecule is revisited to assess the contribution of various algorithmic stages, although similar observations hold for the cyclo[18]carbon molecule as well. At each self-consistent field iteration, the following steps are executed, with each step delivering an output for the next one: (i) the Kohn–Sham equation is solved for the orbitals, (ii) the density is updated through mixing, (iii)

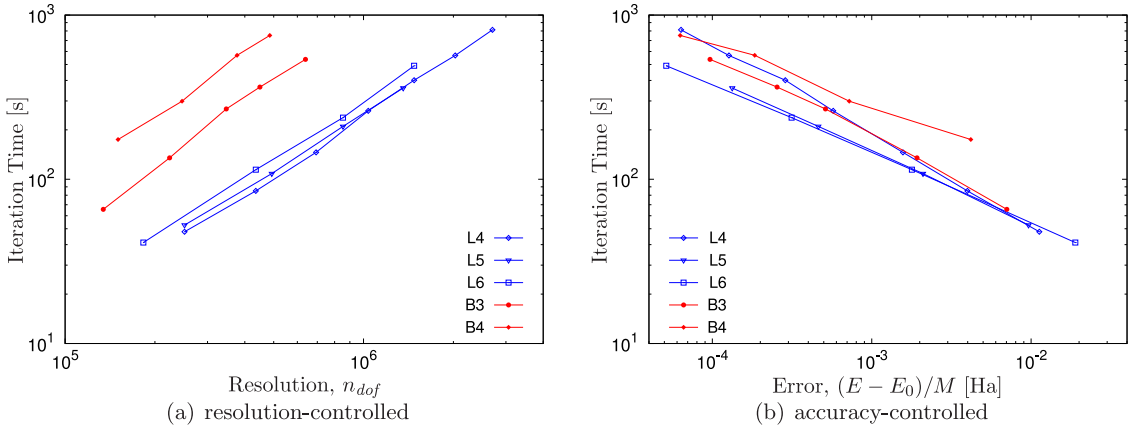

(a) resolution-controlled (b) accuracy-controlled

Fig. 10. The total time for an iteration is summarized.

the Poisson equation is solved for the electrostatic potential, and (iv) the energy is evaluated. The first and third steps dominate the iteration time. The element-level calculations for both of these steps require similar times so that only the one associated with the first step will be monitored. For a given type of discretization and resolution, the order of the Chebyshev filter that is employed in the first step is an additional factor which influences the iteration time, finer resolutions typically requiring higher filter orders to attain convergence of the iterations in a shorter time. During the convergence analysis of the molecular examples in Section 6.3.2, the filter order was initially chosen as 10 and subsequently gradually increased with resolution up to a common value of 60 in all cases. The determination of the optimal filter order towards the minimization of the overall calculation time is not straightforward [84] and can certainly influence the optimality of the discretization type chosen. Presently, because the cost of filtering scales linearly with the filter order, a fixed value of 10 will be chosen in order to assess filtering times. The contributions of the Lanczos and the Rayleigh–Ritz algorithms to the overall cost of the generalized eigenvalue problem solution are omitted because they are less than an order of magnitude smaller than the filtering cost for the problem sizes considered. In the context of a generalized eigenvalue problem, Chebyshev filtering also requires the calculation of the overlap matrix inverse and its operation on vectors within the recursive application of $[M]^{-1}[H]$. For this purpose, the sparse direct solver PARDISO [85] is employed to factorize $[M]$ only once in a preprocessing step and store it in memory for subsequent multiple uses through a finalization step that requires a significantly smaller time. Both of these times will also be reported to further clarify the overall calculation cost. The Poisson equation is also solved in a similar fashion, where the discrete Laplacian is factorized once and invoked from memory in subsequent finalization steps. The times involved are comparable to the ones for the overlap matrix so that only the overlap matrix times will be reported, which are measured from the L_2-projection step in generating the updated initial guess on a refined mesh as remarked in Section 4.2. To summarize, in addition to the total time per iteration, the absolute time measurements corresponding to the following steps will be reported: factorization, finalization, element calculation and filtering. Each measurement is run on a standard workstation with OpenMP parallelization via 32 threads and repeated five times to alleviate the differences observed via averaging.

The total time per iteration for different discretization choices is summarized in Fig. 10. For a given number of degrees of freedom, Lagrange discretizations display similar times whereas the difference between these and B-spline discretizations, as well as the difference among different B-spline choices, are significantly larger. In view of the convergence analysis in Fig. 8(b), it is more informative to monitor the calculation times for a target accuracy. As noted earlier in Section 6.3.2, all times are at the same order of magnitude. Moreover, the cubic B-spline discretization is more efficient than the quartic one in the context of the present implementation and it competes well with the quartic Lagrange discretization. However, Lagrange discretizations of higher order are slightly faster in general. In order to elucidate this difference, additional calculation times are summarized in Fig. 11. Although the factorization step is carried out only once, it is observed that the required times are comparable with the filtering step. Considering that higher filter orders were employed to attain low errors in Fig. 8(b), the overall cost of factorization is not significant within the present setup. The finalization step is indicative of the Poisson equation solution time

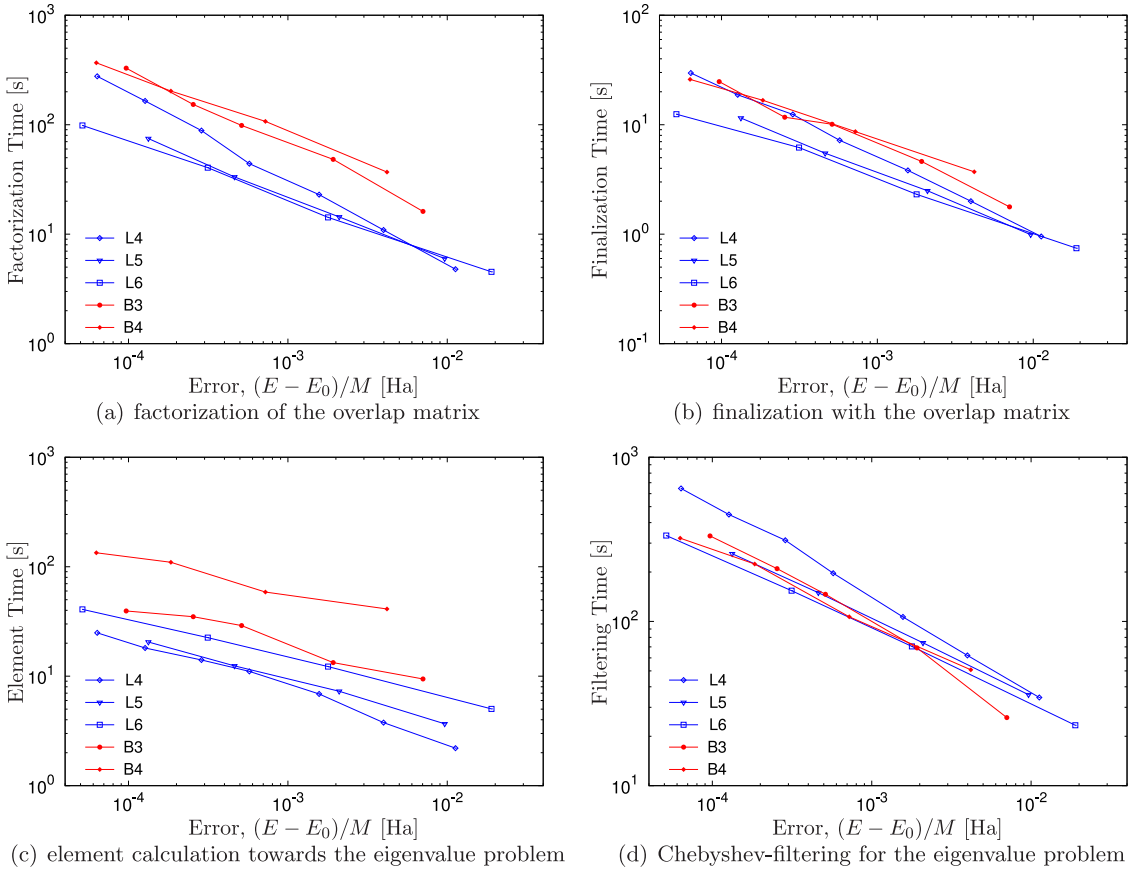

(a) factorization of the overlap matrix
(b) finalization with the overlap matrix
(c) element calculation towards the eigenvalue problem
(d) Chebyshev-filtering for the eigenvalue problem

Fig. 11. Representative factors which influence the calculation times are summarized.

which, along with the element-level calculations, is likewise not significant compared to filtering. On the other hand, the costly filtering step is where B-spline discretizations compete well with Lagrange discretizations, contributing to an improved iteration time for cubic B-splines in particular.

Clearly, as noted in Section 7, if the discrete Kohn–Sham equation could be cast in a standard setting for B-spline discretization as well, this discussion would be considerably influenced. Again for the present low filter order, corresponding filtering times were probed by simply lumping the overlap matrix in order to generate a standard eigenvalue problem by making use of the strictly non-negative entries for B-spline discretizations. In such a setting, the filtering time scales linearly with the number of degrees of freedom. Consequently, the time gain in the transition from the generalized to the standard setting increases with increasing resolution. According to the probed times (not shown), this gain did not exceed a factor of eight for the finest cubic B-spline discretization but would be more significant for larger system sizes. Moreover, such a reduction is sufficient to bring the cost of filtering to the same level with the remaining algorithmic stages. Factorization in preprocessing would then also be a significant overhead that can be entirely eliminated by additionally switching to an iterative solver for the Poisson problem. These would enable assessing the competitiveness of B-spline discretizations in comparison to the Lagrange discretizations employed in [25] for larger system sizes.

References

[1] R.M. Martin, Electronic Structure: Basis Theory and Practical Methods, Cambridge, 2004.
[2] D. Marx, J. Hutter, Ab Initio Molecular Dynamics, Cambridge, 2009.
[3] R. Phillips, Crystals, Defects and Microstructures: Modeling Across Scales, Cambridge, 2001.
[4] R.G. Parr, W. Yang, Density-Functional Theory of Atoms and Molecules, Oxford, 1989.
[5] L. Lin, J. Lu, L. Ying, Numerical methods for Kohn-Sham density functional theory, Acta Numer. 28 (2019) 405–539.

[6] S. Goedecker, Linear scaling electronic structure methods, Rev. Modern Phys. 71 (1999) 1085–1123.
[7] T.L. Beck, Real-space mesh techniques in density-functional theory, Rev. Modern Phys. 72 (2000) 1041–1080.
[8] T. Torsti, T. Eirola, J. Enkovaara, T. Hakala, P. Havu, V. Havu, T. Höynälänmaa, J. Ignatius, M. Lyly, I. Makkonen, T.T. Rantala, J. Ruokolainen, K. Ruotsalainen, E. Räsänen, H. Saarikoski, M.J. Puska, Three real-space discretization techniques in electronic structure calculations, Phys. Status Solidi b 243 (5) (2006) 1016–1053.
[9] J.R. Chelikowsky, N. Troullier, Y. Saad, Finite-difference-pseudopotential method: Electronic structure calculations without a basis, Phys. Rev. Lett. 72 (1994) 1240–1243.
[10] N.A. Modine, G. Zumbach, E. Kaxiras, Adaptive-coordinate real-space electronic-structure calculations for atoms, molecules, and solids, Phys. Rev. B 55 (1997) 10 289.
[11] L. Genovese, A. Neelov, S. Goedecker, T. Deutsch, S.A. Ghasemi, A. Willand, D. Caliste, O. Zilberberg, M. Rayson, A. Bergman, R. Schneider, Daubechies wavelets as a basis set for density functional pseudopotential calculations, J. Chem. Phys. 129 (1) (2008) 014109.
[12] L. Genovese, B. Videau, M. Ospici, T. Deutsch, S. Goedecker, J-F. Méhaut, Daubechies wavelets for high performance electronic structure calculations: The bigdft project, C. R. Mec. 339 (2011) 149–164.
[13] J.E. Pask, P.A. Sterne, Finite element methods in *ab initio* electronic structure calculations, Modelling Simulation Mater. Sci. Eng. 13 (2005) R71–R96.
[14] P. Motamarri, S. Das, S. Rudrarju, K. Ghosh, D. Davydov, V. Gavini, DFT-FE – a massively parallel adaptive finite-element code for large-scale density functional theory calculations, Comput. Phys. Comm. 246 (2020) 106853.
[15] V. Michaud-Rioux, L. Zhang, H. Guo, RESCU: A real space electronic structure method, J. Comput. Phys. 307 (2016) 593–613.
[16] E. Tsuchida, M. Tsukada, Electronic-structure calculations based on the finite-element method, Phys. Rev. B 52 (1995) 5573–5578.
[17] S. Das, P. Motamarri, V. Gavini, B. Turcksin, Y-W. Li, B. Leback, Fast, scalable and accurate finite-element based ab initio calculations using mixed precision computing: 46 PFLOPS simulation of a metallic dislocation system, in: Proceedings of the International Conference for High Performance Computing, Networking, Storage and Analysis, in: SC '19, Association for Computing Machinery, New York, NY, USA, 2019.
[18] J.-L. Fattebert, R.D. Hornung, A.M. Wissing, Finite element approach for density functional theory calculations on locally-refined meshes, J. Comput. Phys. 223 (2007) 759–773.
[19] D. Zhang, L. Shen, A. Zhou, X.-G. Gong, Finite element method for solving Kohn-Sham equations based on self-adaptive tetrahedral mesh, Phys. Lett. A 372 (2008) 5071–5076.
[20] E.J. Bylaska, M. Holst, J.H. Weare, Adaptive finite element method for solving the exact Kohn-Sham equation of density functional theory, J. Chem. Theory Comput. 5 (2009) 937–948.
[21] P. Suryanarayana, V. Gavini, T. Blesgen, K. Bhattacharya, M. Ortiz, Non-periodic finite-element formulation of Kohn-Sham density functional theory, J. Mech. Phys. Solids 58 (2010) 256–280.
[22] G. Bao, G. Hu, D. Liu, An h-adaptive finite element solver for the calculations of the electronic structure, J. Comput. Phys. 4967 (2012) 4967–4979.
[23] G. Hu, H. Xie, F. Xu, A multilevel correction adaptive finite element method for Kohn-Sham equation, J. Comput. Phys. 355 (2018) 436–449.
[24] J. Fang, X. Gao, A. Zhou, A Kohn-Sham equation solver based on hexahedral finite elements, J. Comput. Phys. 231 (2012) 3166–3180.
[25] P. Motamarri, M.R. Nowak, K. Leiter, J. Knap, V. Gavini, Higher-order adaptive finite-element methods for Kohn-Sham density functional theory, J. Comput. Phys. 253 (2013) 308–343.
[26] V. Schauer, C. Linder, All-electron Kohn-Sham density functional theory on hierarchic finite element spaces, J. Comput. Phys. 250 (2013) 644–664.
[27] D. Davydov, T.D. Young, P. Steinmann, On the adaptive finite element analysis of the Kohn-Sham equations: methods, algorithms and implementation, In. J. Numer. Meth. Engng. 106 (2016) 863–888.
[28] W. Koch, M.C. Holthausen, A Chemist's Guide To Density Functional Theory, second ed., Wiley-VCH, 2001.
[29] J.P. Perdew, K. Burke, M. Ernzerhof, Generalized gradient approximation made simple, Phys. Rev. Lett. 77 (1996) 3865–3868.
[30] A. Willand, Y.O. Kvashnin, L. Genovese, Á. Vázquez-Mayagoitia, A.K. Deb, A. Sadeghi, T. Deutsch, S. Goedecker, Norm-conserving pseudopotentials with chemical accuracy compared to all-electron calculations, J. Chem. Phys. 138 (2013) 104109.
[31] Kurt Lejaeghere, Gustav Bihlmayer, Torbjörn Björkman, Peter Blaha, Stefan Blügel, Volker Blum, Damien Caliste, Ivano E. Castelli, Stewart J. Clark, Andrea Dal Corso, Stefano de Gironcoli, Thierry Deutsch, John Kay Dewhurst, Igor Di Marco, Claudia Draxl, Marcin Dułak, Olle Eriksson, José A. Flores-Livas, Kevin F. Garrity, Luigi Genovese, Paolo Giannozzi, Matteo Giantomassi, Stefan Goedecker, Xavier Gonze, Oscar Grånäs, E.K.U. Gross, Andris Gulans, François Gygi, D.R. Hamann, Phil J. Hasnip, N.A.W. Holzwarth, Diana Iuşan, Dominik B. Jochym, François Jollet, Daniel Jones, Georg Kresse, Klaus Koepernik, Emine Küçükbenli, Yaroslav O. Kvashnin, Inka L.M. Locht, Sven Lubeck, Martijn Marsman, Nicola Marzari, Ulrike Nitzsche, Lars Nordström, Taisuke Ozaki, Lorenzo Paulatto, Chris J. Pickard, Ward Poelmans, Matt I.J. Probert, Keith Refson, Manuel Richter, Gian-Marco Rignanese, Santanu Saha, Matthias Scheffler, Martin Schlipf, Karlheinz Schwarz, Sangeeta Sharma, Francesca Tavazza, Patrik Thunström, Alexandre Tkatchenko, Marc Torrent, David Vanderbilt, Michiel J. van Setten, Veronique Van Speybroeck, John M. Wills, Jonathan R. Yates, Guo-Xu Zhang, Stefaan Cottenier, Reproducibility in density functional theory calculations of solids, Science 351 (2016) aad3000.
[32] T.J.R. Hughes, J.A. Cottrell, Y. Bazilevs, Isogeometric analysis: CAD, finite elements, NURBS, exact geometry and mesh refinement, Comput. Methods Appl. Mech. Engrg. 194 (2005) 4135–4195.
[33] J.A. Cottrell, T.J.R. Hughes, Y. Bazilevs, Isogeometric Analysis, Wiley, 2009.
[34] E. Tsuchida, M. Tsukada, Adaptive finite-element method for electronic-structure calculations, Phys. Rev. B 54 (1996) 7602–7605.
[35] H. Bachau, E. Cormier, P. Decleva, J.E. Hansen, F. Martín, Applications of B-splines in atomic and molecular physics, Rep. Progr. Phys. 64 (2001) 1815–1942.

[36] E. Tsuchida, Y.-K. Choe, T. Ohkubo, An adaptive finite-element method for large-scale *ab initio* molecular dynamics simulations, Phys. Chem. Chem. Phys. 17 (2015) 31444–31452.
[37] Z. Romanowski, A B-spline finite element solution of the Kohn-Sham equation for an atom, Modelling Simul. Mater. Sci. Eng. 16 (2008) 015003.
[38] Z. Romanowski, B-spline solver for one-electron Schrödinger equation, Mol. Phys. 109 (2011) 2679–2691.
[39] A. Masud, R. Kannan, B-splines and NURBS based finite element methods for Kohn-Sham equations, Comput. Methods Appl. Mech. Engrg. 241–244 (2012) 112–127.
[40] R. Cimrman, M. Novák, R. Kolman, M. Tůma, J. Vackář, Isogeometric analysis in electronic structure calculations, Math. Comput. Simulation 145 (2018) 125–135.
[41] R. Cimrman, M. Novák, R. Kolman, M. Tůma, J. Plešek, J. Vackář, Convergence study of isogeometric analysis based on Bézier extraction in electronic structure calculations, Appl. Math. Comput. 319 (2018) 138–152.
[42] A. Masud, A.A. Al-Naseem, R. Kannan, H. Gajendran, B-splines and NURBS based finite element methods for strained electronic structure calculations, J. Appl. Mech. 85 (2018) 091009.
[43] İ. Temizer, P. Motamarri, V. Gavini, NURBS-Based non-periodic finite element framework for Kohn-Sham density functional theory, J. Comput. Phys. 410 (2020) 109364.
[44] M.R. Dörfel, B. Jüttler, B. Simeon, Adaptive isogeometric analysis by local h-refinement with T-splines, Comput. Methods Appl. Mech. Engrg. 199 (2010) 264–275.
[45] A.-V. Vuong, C. Giannelli, B. Jüttler, B. Simeon, A hierarchical approach to adaptive local refinement in isogeometric analysis, Comput. Methods Appl. Mech. Engrg. 200 (2011) 3554–3567.
[46] K.A. Johannessen, T. Kvamsdal, T. Dokken, Isogeometric analysis using LB B-splines, Comput. Methods Appl. Mech. Engrg. 269 (2014) 471–514.
[47] M.A. Scott, D.C. Thomas, E.J. Evans, Isogeometric spline forests, Comput. Methods Appl. Mech. Engrg. 269 (2014) 222–264.
[48] C. Bracco, A. Buffa, C. Giannelli, R. Vázquez, Adaptive isogeometric methods with hierarchical splines: an overview, Discrete Contin. Dyn. Syst. 39 (2019) 241–261.
[49] B. Kanungo, V. Gavini, Large-scale all-electron density functional theory calculations using an enriched finite-element basis, Phys. Rev. B 95 (2017) 035113.
[50] J.E. Pask, N. Sukumar, Partition of unity finite element method for quantum mechanical materials calculations, Extrem. Mech. Lett. 11 (2017) 8–17.
[51] N. Sukumar, J.E. Pask, Classical and enriched finite element formulations for Bloch-periodic boundary conditions, Internat. J. Numer. Methods Engrg. 77 (2009) 1121–1138.
[52] C. Albrecht, C. Klaar, J.E. Pask, M.A. Schweitzer, N. Sukumar, A. Zeigenhagel, Orbital-enriched flat-top partition of unity method for the Schrödinger eigenproblem, Comput. Methods Appl. Mech. Engrg. 342 (2018) 224–239.
[53] X. Gonze, R. Stumpf, M. Scheffler, Analysis of separable potentials, Phys. Rev. B 44 (1991) 8503–8513.
[54] W.E. Pickett, Pseudopotential methods in condensed matter applications, Comput. Phys. Rep. 9 (1989) 115–198.
[55] J.E. Pask, P.A. Sterne, Real-space formulation of the electrostatic potential and total energy of solids, Phys. Rev. B 71 (2005) 113101.
[56] J.E. Pask, N. Sukumar, S.E. Mousavi, Linear scaling solution of the all-electron Coulomb problem in solids, J. Multiscale Comput. Eng. 10 (2012) 83–99.
[57] J.P. Perdew, K. Burke, Comparison shopping for a gradient-corrected density functional, J. Quantum Chem. 57 (1996) 309–319.
[58] M.A.L. Marques, M.J.T. Oliveira, T. Burnus, Libxc: a library of exchange and correlation functionals for density functional theory, Comput. Phys. Comm. 183 (2012) 2272–2281.
[59] D. Porezag, M.R. Pederson, A.Y. Liu, The importance of nonlinear core corrections for density-functional based pseudopotential calculations, Phys. Rev. B 60 (1999) 14132–14139.
[60] S.G. Louie, S. Froyen, M.L. Cohen, Nonlinear ionic pseudopotentials in spin-density-functional calculations, Phys. Rev. B 26 (1982) 1738–1742.
[61] D.R. Hamann, M. Schlüter, C. Chiang, Norm-conserving pseudopotentials, Phys. Rev. Lett. 43 (1979) 1494–1497.
[62] L. Kleinman, D.M. Bylander, Efficacious form for model seudopotentials, Phys. Rev. Lett. 48 (1982) 1425–1428.
[63] P.E. Blöchl, Generalized separable potentials for electronic-structure calculations, Phys. Rev. B 41 (1990) 5414–5416.
[64] D.R. Hamann, Optimized norm-conserving Vanderbilt pseudopotentials, Phys. Rev. B 88 (2013) 085117.
[65] D. Vanderbilt, Soft self-consistent pseudopotentials in a generalized eigenvalue formalism, Phys. Rev. B 41 (1990) 7892–7895.
[66] S. Goedecker, M. Teter, J. Hutter, Separable dual-space Gaussian pseudopotentials, Phys. Rev. B 54 (1996) 1703–1710.
[67] M. Fuchs, M. Scheffler, Ab initio pseudopotentials for electronic structure calculations of poly-atomic systems using density-functional theory, Comput. Phys. Comm. 119 (1999) 67–98.
[68] C. Hartwigsen, S. Goedecker, J. Hutter, Relativistic separable dual-space Gaussian pseudopotentials from h to rn, Phys. Rev. B 58 (1998) 3641–3662.
[69] M. Krack, Pseudopotentials for H to Kr optimized for gradient-corrected exchange-correlation functionals, Theor. Chem. Acc. 114 (2005) 145–152.
[70] BigDFT website, New Soft-Accurate NLCC pseudopotentials, http://bigdft.org/Wiki/index.php?title=New_Soft-Accurate_NLCC_pseudopotentials&oldid=2586. (Accessed 9 October 2019).
[71] R. Zhuravel, H. Huang, G. Polycarpou, S. Polydorides, P. Motamarri, L. Katrivas, D. Rotem, J. Sperling, L. Zotti, A. Kotlyar, J. Cuevas, V. Gavini, S. Skourtis, D. Porath, Backbone charge transport in double-stranded DNA, Nature Nanotechnol. 15 (2020) 1–5, http://dx.doi.org/10.1038/s41565-020-0741-2.
[72] Y. Zhou, Y. Saad, M.L. Tiago, J.R. Chelikowsky, Self-consistent-field calculations using Chebyshev-filtered subspace iteration, J. Comput. Phys. 219 (2006) 172–184.

[73] Y. Zhou, J.R. Chelikowsky, Y. Saad, Chebyshev-Filtered subspace iteration method free of sparse diagonalization for solving the Kohn-Sham equation, J. Comput. Phys. 274 (2014) 770–782.
[74] A.S. Banerjee, R.S. Elliott, R.D. James, A spectral scheme for Kohn-Sham density functional theory of clusters, J. Comput. Phys. 287 (2015) 226–253.
[75] Y. Saad, Numerical Methods for Large Eigenvalue Problems, second ed., SIAM, 2011.
[76] R.M. Dreizler, E.K.U. Gross, Density Functional Theory: An Approach To the Quantum Many-Body Problem, Springer, 1990.
[77] G. Kresse, J. Furthmüller, Efficient iterative schemes for *ab initio* total-energy calculations using a plane-wave basis set, Phys. Rev. B 54 (1996) 11169–11186.
[78] D.J. Griffiths, Introduction To Quantum Mechanics, second ed., Pearson, 2005.
[79] ATOM website, Density functional calculations for atoms with generation and testing of different pseudopotentials, http://bohr.inesc-mn.pt/~jlm/pseudo.html. (Accessed 1 October 2019) (version 5.803).
[80] X. Gonze, F. Jollet, F. Abreu Araujo, D. Adams, B. Amadon, T. Applencourt, C. Audouze, J.-M. Beuken, J. Bieder, A. Bokhanchuk, E. Bousquet, F. Bruneval, D. Caliste, M. Côté, F. Dahm, F. Da Pieve, M. Delaveau, M. Di Gennaro, B. Dorado, C. Espejo, G. Geneste, L. Genovese, A. Gerossier, M. Giantomassi, Y. Gillet, D.R. Hamann, L. He, G. Jomard, J. Laflamme Janssen, S. Le Roux, A. Levitt, A. Lherbier, F. Liu, I. Lukačević, A. Martin, C. Martins, M.J.T. Oliveira, S. Poncé, Y. Pouillon, T. Rangel, G.-M. Rignanese, A.H. Romero, B. Rousseau, O. Rubel, A.A. Shukri, M. Stankovski, M. Torrent, M.J. Van Setten, B. Van Troeye, M.J. Verstraete, D. Waroquiers, J. Wiktor, B. Xu, A. Zhou, J.W. Zwanziger, Recent developments in the ABINIT software package, Comput. Phys. Comm. 205 (2016) 106–131, http://dx.doi.org/10.1016/j.cpc.2016.04.003, https://doi.org/10.1016/j.cpc.2016.04.003.
[81] S. Mohr, L.E. Ratcliff, L. Genovese, D. Caliste, P. Boulanger, S. Goedecker, T. Deutsch, Accurate and efficient linear scaling DFT calculations with universal applicability, Phys. Chem. Chem. Phys. 17 (2015) 31360–31370.
[82] K. Kaiser, L.M. Scriven, F. Schulz, P. Gawel, L. Gross, H.L. Anderson, An sp-hybridized molecular carbon allotrope, cyclo[18]carbon, Science 365 (2019) 1299–1301.
[83] F. Diederich, Y. Rubin, C.B. Knobler, R.L. Whetten, K.E. Schriver, K.N. Houk, Y. Li, All-carbon molecules: evidence for the generation of cyclo[18]carbon from a stable organic precursor, Science 245 (1989) 1088–1090.
[84] A. Breuer, X.-C. Wang, More robust Chebyshev filtering for SCF iteration, with applications in real-space DFT, J. Comput. Phys. 374 (2018) 27–46.
[85] M. Bollhöfer, O. Schenk, R. Janalik, S. Hamm, K. Gullapalli, State-of-the-art sparse direct solvers, in: A. Grama, A.H. Sameh (Eds.), Parallel Algorithms in Computational Science and Engineering, Springer, 2020, pp. 3–33.